

# Integrated Sensing and Communications in Clutter Environment

Hongliang Luo, Yucong Wang, Jianwei Zhao, Huihui Wu, Shaodan Ma and Feifei Gao

**Abstract**—In this paper, we propose a practical integrated sensing and communications (ISAC) framework to sense dynamic targets from clutter environment while ensuring users communications quality. To implement communications function and sensing function simultaneously, we design multiple communications beams that can communicate with the users as well as one sensing beam that can rotate and scan the entire space. To minimize the interference of sensing beam on existing communications systems, we divide the service area into *sensing beam for sensing (S4S) sector* and *communications beam for sensing (C4S) sector*, and provide beamforming design and power allocation optimization strategies for each type sector. Unlike most existing ISAC studies that ignore the interference of static environmental clutter on target sensing, we construct a mixed sensing channel model that includes both static environment and dynamic targets. When base station receives the echo signals, the mean phasor cancellation (MPC) method is employed to filter out the interference from static environmental clutter and to extract the effective dynamic target echoes. Then a complete and practical dynamic target sensing scheme is designed to detect the presence of dynamic targets and to estimate their angles, distances, and velocities. In particular, dynamic target detection and angle estimation are realized through angle-Doppler spectrum estimation (ADSE) and joint detection over multiple subcarriers (MSJD), while distance and velocity estimation are realized through the extended subspace algorithm. Simulation results demonstrate the effectiveness of the proposed scheme and its superiority over the existing methods that ignore environmental clutter.

**Index Terms**—Integrated sensing and communications, dynamic target sensing, static environment sensing, clutter suppression, power allocation.

## I. INTRODUCTION

Integrated sensing and communications (ISAC) has recently attracted significant research interest in the field of wireless communications [1]–[3]. The idea is to utilize communication signals to sense various information in real physical world, such as architectural composition, human activity, etc, while ensuring users communications quality. Since ISAC allows sensing systems and communication systems to share the same hardware and spectrum resources, and can serve various intelligent applications, such as vehicle-to-everything, digital twins, etc., it has been deemed as one of the key technologies for sixth generation (6G) communications [4], [5].

Hongliang Luo, Yucong Wang, Huihui Wu and Feifei Gao are with Department of Automation, Tsinghua University, Beijing 100084, China (email: luohl23@mails.tsinghua.edu.cn; wangyuco21@mails.tsinghua.edu.cn; hhwu1994@mail.tsinghua.edu.cn; feifeigao@ieee.org).

Jianwei Zhao is with the High-Tech Institute of Xi’an, Xi’an 710025, China (e-mail: zhaojianeip@163.com).

Shaodan Ma is with the State Key Laboratory of Internet of Things for Smart City and the Department of Electrical and Computer Engineering, University of Macau, Macao S.A.R. 999078, China (e-mail: shaodanma@um.edu.mo).

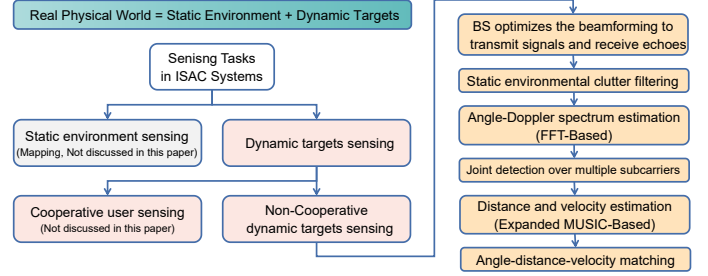


Fig. 1. ISAC sensing task classification and flowchart of the proposed sensing echo signals processing process.

The ultimate functionality of sensing is to construct the mapping relationship from the *real physical world* to the *digital twin world*, where the former includes static environment (such as roads and buildings) and dynamic targets (such as pedestrians and vehicles). Therefore, the sensing tasks in ISAC systems include *static environment sensing (SES)* and *dynamic targets sensing (DTS)* as shown in the left half of Fig. 1. The changes of static environment are usually slow, and thus one can apply various environmental reconstruction techniques to sense the static environment [6]–[8]. However, since the changes of dynamic targets are rapid, it is necessary to detect the presence of dynamic targets and update their parameter estimates in real-time. Generally, one can divide the DTS problem into two categories: (1) sensing cooperative communications users, e.g., mobile phones; and (2) sensing non-cooperative dynamic targets that are not communicating with the base station (BS), e.g., moving objects or mobile users not in communication status.

In addition, with the increasing demand for sensing, researchers are committed to making ISAC systems possess ultra-high sensing accuracy. Encouragingly, sensing in mmWave or Terahertz band with massive multiple input and multiple output (MIMO) array can achieve higher accuracy thanks to its high directivity and high temporal resolution [9], [10]. Therefore, the massive MIMO based ISAC systems have been widely studied. For the aspect of sensing cooperative communication users, the users’ positions can be estimated by processing the communications signals and extracting the channel parameters, such as time of arrival (TOA), angle of departure (AOD), etc [11]–[14]. On the other side, sensing non-cooperative target has also been studied under ISAC framework. For example, Z. Gao *et al.* proposed an ISAC system relying on MIMO array, which applied compressed sampling to facilitate target sensing and other ISAC processing [15]. Z. Wang *et al.* proposed a simultaneously transmitting

and reflecting surface enabled ISAC framework, in which the two-dimensional maximum likelihood estimation was utilized to estimate target angle [16]. Y. Li *et al.* proposed a two-stage algorithm to estimate the positions and velocities of multiple targets with orthogonal frequency division multiplexing (OFDM) signals [17]. P. Kumari *et al.* proposed an ISAC system working for the internet of vehicles, which realized vehicle to vehicle communication and full duplex radar sensing [18]. X. Chen *et al.* proposed a multiple signal classification based ISAC system that can attain high estimation accuracy for dynamic target sensing [19]. However, all these works ignore the interference caused by static environmental clutter on dynamic target sensing, which does not match the real scenarios where the targets are always submerged by the interference of static environment and are difficult to separate from it, thus limiting the sensing performance in the real scenarios.

Meanwhile, for ISAC systems based on MIMO arrays, one should design the beamforming with multiple beams to implement communications function and sensing function simultaneously [20]–[23]. For example, C. B. Barneto *et al.* formulated one beamforming design problem in multi-user ISAC system, aiming to maximize the power at the sensing direction while remain certain power at the communications directions [24]. H. Luo *et al.* proposed an ISAC system that combined BS and reconfigurable intelligence surface (RIS), and optimized the beamforming matrix jointly to maximize the achievable sum-rate of communication users while meeting the sensing beam constraints [25]. X. Wang *et al.* investigated the partially-connected beamforming design for multi-user ISAC systems, aiming to maximize the Cramer-Rao bound of DOA estimation while ensuring communications performance [26]. However, all these works require complex optimization processes and are difficult to implement in practical systems.

In this paper, we propose a practical ISAC framework to sense the dynamic targets from the clutter environment while ensuring users communications quality. The contributions of this paper are summarized as follows.

- We propose a practical ISAC framework to implement communications and sensing simultaneously, in which we design multiple communications beams that can communicate with the users while assign one sensing beam that can rotate and scan the entire space. The entire process is summarized in the right half of Fig. 1.
- BS should optimize the transmitting beamforming during each time slot to transmit signals. Specifically, to minimize the interference of sensing beam on existing communications systems, we divide the service area of BS into *sensing beam for sensing (S4S) sectors* and *communications beam for sensing (C4S) sectors*. To avoid complex optimizations that are difficult to implement in practical systems, we transform the precoding optimization problem into a power allocation problem for communications and sensing beams, and provide effective power allocation strategies for each type sector.
- We construct clutter environment model for practical ISAC systems, and then the echoes received by BS includes both the echoes caused by static environment



Fig. 2. System model.

and the echoes caused by dynamic targets. To address the negative interference of static environmental clutter on dynamic target sensing, we employ the mean phasor cancellation (MPC) method to filter out the interference from static environmental clutter and to extract the effective dynamic target echoes. Then angle-Doppler spectrum estimation (ADSE) and joint detection over multiple sub-carriers (MSJD) are proposed to detect the dynamic targets and to estimate their angles. The extended subspace algorithm is utilized to estimate distances and velocities of dynamic targets. Besides, in order to obtain multiple parameters for each target, we design an angle-distance-velocity matching method to realize parameters matching.

- Various simulations are provided to demonstrate the effectiveness of the proposed schemes and its superiority over existing methods that ignore environmental clutter.

The remainder of this paper is organized as follows. In Section II, we propose a practical ISAC framework that effectively integrates the sensing functions into the existing communications systems. In Section III, we provide a low complexity and practical beamforming design and power allocation strategy. Then we design a complete and practical scheme to sense the dynamic targets from the clutter environment in Section IV. Simulation results and conclusions are given in Section V and Section VI, respectively.

*Notation:* Lower-case and upper-case boldface letters  $\mathbf{a}$  and  $\mathbf{A}$  denote a vector and a matrix;  $\mathbf{a}^T$  and  $\mathbf{a}^H$  denote the transpose and the conjugate transpose of vector  $\mathbf{a}$ , respectively;  $[\mathbf{a}]_n$  denotes the  $n$ -th element of the vector  $\mathbf{a}$ ;  $[\mathbf{A}]_{i,j}$  denotes the  $(i,j)$ -th element of the matrix  $\mathbf{A}$ ;  $\mathbf{A}[i_1 : i_2, :]$  is the submatrix composed of all columns elements in rows  $i_1$  to  $i_2$  of matrix  $\mathbf{A}$ ;  $\mathbf{A}[:, j_1 : j_2]$  is the submatrix composed of all rows elements in columns  $j_1$  to  $j_2$  of matrix  $\mathbf{A}$ ;  $|\cdot|$  denotes the absolute operator;  $\text{eig}(\cdot)$  represents the matrix eigenvalue decomposition function.

## II. SYSTEM MODEL AND PROPOSED ISAC FRAMEWORK

In this section, we will propose a practical ISAC framework that effectively integrates the sensing functions into the existing communications systems.

### A. BS Model

A massive MIMO based ISAC system operating in mmWave or Terahertz frequency bands with OFDM modulation is

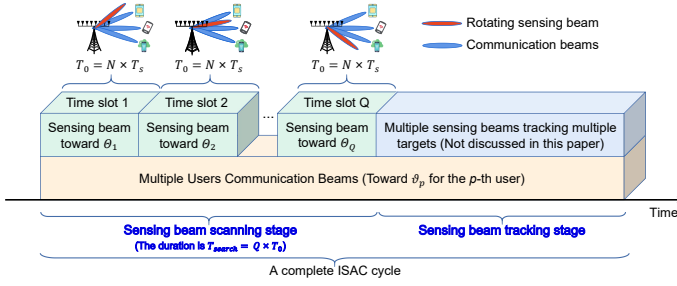


Fig. 3. The proposed ISAC framework.

depicted in Fig. 2, which employs a dual function BS for wireless communication and radar sensing at the same time. The BS is configured with two parallel and closely placed uniform linear arrays (ULAs) of  $N_T$  and  $N_R$  antenna elements as transmitting array and receiving array, respectively, in which the antenna spacing is  $d \leq \frac{\lambda}{2}$  and  $\lambda$  is the wavelength. Assuming that the ULAs are parallel to the y-axis, and the antenna indices in the transmitting- and receiving- ULAs are  $0, \dots, N_T - 1$  and  $0, \dots, N_R - 1$ . Suppose that the communications system uses OFDM signals with  $M$  subcarriers in total, and the lowest frequency and the subcarrier interval are  $f_0$  and  $\Delta f$ , respectively. Then the transmission bandwidth is  $W = (M - 1)\Delta f$ , and the frequency of the  $m$ -th subcarrier is  $f_m = f_0 + m\Delta f$ , where  $m = 0, 1, \dots, M - 1$ .

Assume that the service area of BS is  $\{(r, \theta) | r_{min} \leq r \leq r_{max}, \theta_{min} \leq \theta \leq \theta_{max}\}$ , and there are  $P$  single-antenna communications users,  $K$  dynamic targets, as well as widely distributed static environment within this area. We assume that the position and radial velocity of the  $k$ -th dynamic target are  $(r_k, \theta_k)$  and  $v_k$ . Besides, we assume that the position of the  $p$ -th user is  $(R_p, \vartheta_p)$ , and suppose that the positions of users are known and are stationary to BS, as the cooperative users' positions can be easily obtained through user reporting, or other techniques [9], [10], [27].

### B. Proposed ISAC Framework

The task of an ISAC system is to sense all  $K$  dynamic targets while serving the communications of all  $P$  users, in which the sensing of dynamic targets includes detection, estimation, and tracking. As described in Fig. 3, the proposed ISAC framework consists of two stages: *sensing beam scanning (SBS) stage* and *sensing beam tracking (SBT) stage*. For the aspect of communications, BS continuously generates  $P$  communications beams towards  $P$  users to maintain communications service during both SBS stage and SBT stage.

For the aspect of sensing, BS generates one sensing beam that can rotate and scan the service area during SBS stage, that is, the sensing beam can explore all angle spaces at certain scanning intervals within a certain period of time, and BS can detect the targets and estimate their parameters during SBS stage. Next, BS should generate one or  $K$  sensing beams to track all  $K$  dynamic targets during SBT stage. In this work, we mainly focus on SBS stage, while SBT stage is a well separate issue and will be discussed in subsequent works.

Suppose that BS adopts  $N$  consecutive OFDM symbols to realize dynamic target sensing in one single direction, and

the OFDM symbol interval time is  $T_s = \frac{1}{\Delta f}$ . As shown in Fig. 3, we divide the SBS stage into  $Q$  transient time slots, and each time slot lasts for a time duration of  $T_0 = N \cdot T_s$ . In the  $q$ -th time slot, BS needs to generate  $P$  communications beams pointing to  $P$  users and generate one sensing beam pointing to the *sensing scanning angle*  $\Theta_q$  from transmitting array. Here we assume that the transmission power of BS is  $P_t$ , the energy of sensing beam is  $\rho_q P_t$ , and the remaining energy  $(1 - \rho_q)P_t$  is evenly distributed to each communications beam, where  $\rho_q \in [0, 1]$ . Then the transmission signals on the  $m$ -th subcarrier of the  $n$ -th OFDM symbol in the  $q$ -th time slot should be represented as

$$\begin{aligned} \mathbf{x}_{q,n,m} &= \sum_{p=1}^P \mathbf{w}_{c,p,q} s_{n,m}^{c,p,q} + \mathbf{w}_{s,q} s_{n,m}^{s,q} \\ &= \sum_{p=1}^P \sqrt{\frac{(1-\rho_q)P_t}{PN_T}} \mathbf{a}_{TX}(\vartheta_p) s_{n,m}^{c,p,q} + \sqrt{\frac{\rho_q P_t}{N_T}} \mathbf{a}_{TX}(\Theta_q) s_{n,m}^{s,q}, \end{aligned} \quad (1)$$

where  $\mathbf{w}_{c,p,q} = \sqrt{\frac{(1-\rho_q)P_t}{PN_T}} \mathbf{a}_{TX}(\vartheta_p)$  and  $\mathbf{w}_{s,q} = \sqrt{\frac{\rho_q P_t}{N_T}} \mathbf{a}_{TX}(\Theta_q)$  are the communications beamforming vector for the  $p$ -th user and the sensing beamforming vector for the  $\Theta_q$ , respectively, and  $\mathbf{a}_{TX}(\theta)$  is the transmitting steering vector for angle  $\theta$  with the form

$$\mathbf{a}_{TX}(\theta) = [1, e^{j2\pi f_0 \frac{d \sin \theta}{c}}, \dots, e^{j2\pi f_0 \frac{(N_T-1)d \sin \theta}{c}}]^T \in \mathbb{C}^{N_T \times 1}. \quad (2)$$

Moreover,  $s_{n,m}^{c,p,q}$  and  $s_{n,m}^{s,q}$  are the communication signals for the  $p$ -th user and the sensing detection signals transmitted by BS through the  $m$ -th subcarrier of the  $n$ -th OFDM symbol in the  $q$ -th time slot. Without loss of generality,  $s_{n,m}^{c,p,q}$  and  $s_{n,m}^{s,q}$  are both assumed as zero-mean, temporally-white and wide-sense stationary stochastic process, and  $s_{n,m}^{c,p,q}$  is uncorrelated with  $s_{n,m}^{s,q}$ . Here, both  $s_{n,m}^{c,p,q}$  and  $s_{n,m}^{s,q}$  are normalized to have unit power, and the actual transmission power will be calculated in the corresponding beamforming vectors.

In addition, to suppress the interference of echoes from other directions, BS also demands to set one sensing receiving beam pointing to  $\Theta_q$  at receiving array. Here we set the receiving beamforming vector in the  $q$ -th time slot as  $\mathbf{w}_{RX,q} = \frac{1}{\sqrt{N_R}} \mathbf{a}_{RX}(\Theta_q)$ , where  $\mathbf{a}_{RX}(\theta)$  is the receiving steering vector for angle  $\theta$  with the form

$$\mathbf{a}_{RX}(\theta) = [1, e^{j2\pi f_0 \frac{d \sin \theta}{c}}, \dots, e^{j2\pi f_0 \frac{(N_R-1)d \sin \theta}{c}}]^T \in \mathbb{C}^{N_R \times 1}. \quad (3)$$

To evenly scan the service area, we set  $\Theta_q = \arcsin[\sin \theta_{min} + (q - 1) \frac{\sin \theta_{max} - \sin \theta_{min}}{Q-1}]$ , where  $q = 1, 2, \dots, Q$ . Then BS will transmit signals through transmitting array and receive echoes through receiving array during each time slot. After completing the beam scanning, we need to design efficient and accurate dynamic target sensing algorithms to detect the dynamic targets and to estimate their angles, distances, and velocities in clutter environment.

### C. Interference Management

During SBS stage, due to the continuous rotation of sensing beam, the intervals between the direction of sensing beam and the directions of communications beams are constantly

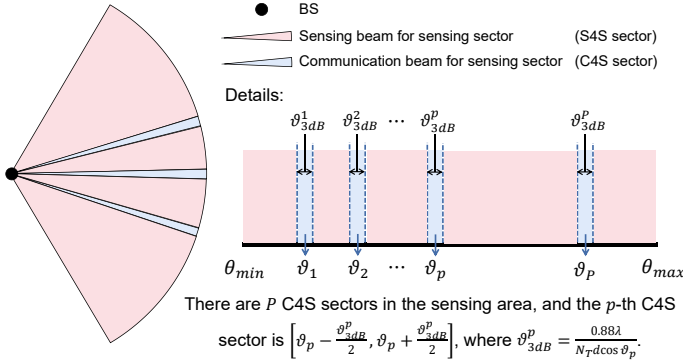


Fig. 4. Schematic diagram of S4S sector and C4S sector.

changing. Hence, sensing beam would bring dynamic interference to communications beams. Specifically, when the sensing scanning angle  $\Theta_q$  is far from user's angle, the interference of sensing beam on communications beams is relatively small. However, when  $\Theta_q$  is close to user's angle, the interference of sensing beam on communications beams is significant large. Especially when the mainlobe of sensing beam overlaps with the mainlobe of communications beam, the sensing beam will cause serious interference to this communications beam. Therefore, we should properly control the power allocated to sensing beam to suppress the dynamic interference.

Intuitively, when  $\Theta_q$  is close to  $\vartheta_p$ , in order to avoid serious interference caused by sensing beam on user, BS should not generate a dedicated sensing beam at this time. Interestingly, as the communications beam for the user can also illuminate the targets in this direction and would also cause echoes, the BS can still utilize the echoes of communications beam itself to sense the targets. Hence we divide the service area of BS into *sensing beam for sensing (S4S) sectors* and *communications beam for sensing (C4S) sectors* as shown in Fig. 4. In general, we construct a protective C4S sector for each user, and the C4S sector corresponding to the  $p$ -th user is  $[\vartheta_p - \frac{\vartheta_{3dB}^p}{2}, \vartheta_p + \frac{\vartheta_{3dB}^p}{2}]$ , where  $\vartheta_{3dB}^p = \frac{0.88\lambda}{N_T d \cos \vartheta_p}$  is the half power beam width<sup>1</sup>. Then we should take the following strategies to suppress the interference of sensing beam on communications beams:

- 1) When  $\Theta_q$  is located within the  $p$ -th C4S sector, we design that the BS does not generate the dedicated sensing beam, but utilizes the communications beam toward  $\vartheta_p$  to illuminate the targets and realize sensing.
- 2) When  $\Theta_q$  is located within S4S sectors, BS needs to optimize  $\rho_q$  for beamforming to maximize sensing performance while ensuring communications performance.

The difficulty of the above design is that the interference of rotating sensing beam on communications beams is dynamically changing during SBS stage. Therefore, BS must carefully and quickly update  $\rho_q$  for each time slot to suppress the interference, which will be addressed in Section III.

#### D. Clutter Environment

Note that the receiving array will receive both the effective echoes caused by interested dynamic targets (dynamic target

echoes) and the undesired echoes caused by uninterested background environment. In radar systems, these undesired echoes are usually referred to as ‘‘clutter’’, including ground clutter, sea clutter, weather clutter, birds clutter, etc [28], [29]. The key difference between dynamic target echoes and clutter lies in their different Doppler frequencies. That is, the Doppler frequency of dynamic target echoes is usually much higher than that of clutter, while the Doppler frequency of clutter is usually zero or a small non-zero value. Specifically, the ground clutter is usually caused by static environment, such as land, mountains, roads, and buildings, etc, and its signal power intensity is usually much higher than that of the dynamic target echo, but its Doppler frequency is almost zero [30], [31]. Hence a practical modeling of echo signals should include both dynamic targets echoes and static environment echoes, and BS needs to accurately detect the dynamic targets and estimate their parameters under clutter environment. However, most existing ISAC works [15]–[19] ignore the interference caused by static environmental clutter on dynamic target sensing, which does not match the real scenarios. We will construct a practical ISAC scene with clutter environment and provide a complete dynamic targets sensing scheme in Section IV.

### III. JOINT COMMUNICATIONS AND SENSING POWER ALLOCATION OPTIMIZATION

In this section, we will jointly optimize ISAC power allocation for each time slot.

#### A. Communication Performance Metric

Let us first describe the communication process. The communications channel of the  $p$ -th user on the  $m$ -th subcarrier of the  $n$ -th OFDM symbol can be represented as

$$\mathbf{h}_{c,p,n,m} = \gamma_p e^{-j2\pi f_m \frac{R_p}{c}} \mathbf{a}_{TX}(\vartheta_p) \in \mathbb{C}^{N_T \times 1}, \quad (4)$$

where  $\gamma_p = \sqrt{\frac{\lambda^2}{(4\pi R_p)^2}}$  is the channel fading for the  $p$ -th user. Then the received communications signal of the  $p^*$ -th user on the  $m$ -th subcarrier of the  $n$ -th symbol in the  $q$ -th time slot is  $y_{n,m}^{c,p^*,q}$ , which is expressed as (5) at the top of next page, where  $\gamma'_{p^*} \triangleq \gamma_{p^*} e^{-j2\pi f_m \frac{R_{p^*}}{c}}$ ,  $n_{n,m}^{c,p^*,q}$  is the zero-mean additive complex Gaussian white noise at the user with variance  $\sigma_{c,p^*}^2$ , and  $F_{TX}(\theta_1, \theta_2) \triangleq \mathbf{a}_{TX}^H(\theta_1) \mathbf{a}_{TX}(\theta_2)$ .

Eq. (5) indicates that the received communications signal is composed of four parts: effective reception (ER), multiple users interference (MUI), sensing interference (SI), and noise (Noise). Note that the sensing beam has a negative interfering effect on the communications beams, and thus the signal-to-interference-plus-noise ratio (SINR) should be used to describe the communications performance. Specifically, the SINR for the  $p^*$ -th user in the  $q$ -th time slot is

$$\text{SINR}_{c,p^*,q} = \frac{\mathbb{E}\{|\text{ER}|^2\}}{\mathbb{E}\{|\text{MUI}|^2\} + \mathbb{E}\{|\text{SI}|^2\} + \mathbb{E}\{|\text{Noise}|^2\}} = \frac{(1-\rho_q)N_T^2}{(1-\rho_q)\sum_{p=1, p \neq p^*}^P G_{TX}(\vartheta_{p^*}, \vartheta_p) + P\rho_q G_{TX}(\vartheta_{p^*}, \Theta_q) + \frac{PN_T\sigma_{c,p^*}^2}{P_t\gamma_{p^*}^2}}, \quad (6)$$

<sup>1</sup>This paper takes  $\vartheta_{3dB}^p$  as a typical value for the width of the C4S sector, which can be adjusted according to actual performance in practical systems.

$$\begin{aligned}
y_{n,m}^{c,p^*,q} &= \mathbf{h}_{c,p^*,n,m}^H \mathbf{x}_{q,n,m} + n_{n,m}^{c,p^*,q} = \gamma'_{p^*} \left[ \sqrt{\frac{(1-\rho_q)P_t}{PN_T}} \sum_{p=1}^P F_{TX}(\vartheta_{p^*}, \vartheta_p) s_{n,m}^{c,p,q} + \sqrt{\frac{\rho_q P_t}{N_T}} F_{TX}(\vartheta_{p^*}, \Theta_q) s_{n,m}^{s,q} \right] + n_{n,m}^{c,p^*,q} \\
&= \underbrace{\gamma'_{p^*} \sqrt{\frac{(1-\rho_q)P_t N_T}{P}} s_{n,m}^{c,p^*,q}}_{\text{ER}} + \underbrace{\gamma'_{p^*} \sqrt{\frac{(1-\rho_q)P_t}{PN_T}} \sum_{p=1, p \neq p^*}^P F_{TX}(\vartheta_{p^*}, \vartheta_p) s_{n,m}^{c,p,q}}_{\text{MUI}} + \underbrace{\gamma'_{p^*} \sqrt{\frac{\rho_q P_t}{N_T}} F_{TX}(\vartheta_{p^*}, \Theta_q) s_{n,m}^{s,q}}_{\text{SI}} + \underbrace{n_{n,m}^{c,p^*,q}}_{\text{Noise}}
\end{aligned} \tag{5}$$

where  $\mathbb{E}\{\cdot\}$  is the mathematical expectation operator and  $G_{TX}(\theta_1, \theta_2)$  is defined as

$$G_{TX}(\theta_1, \theta_2) = |F_{TX}(\theta_1, \theta_2)|^2 = \left| \frac{\sin[\frac{\pi d f_0}{c}(\sin \theta_1 - \sin \theta_2) N_T]}{\sin[\frac{\pi d f_0}{c}(\sin \theta_1 - \sin \theta_2)]} \right|^2. \tag{7}$$

### B. Sensing Performance Metric

To facilitate the optimization of the transmitting beams, we define the array response matrix of the transmitting and receiving array at the sensing scanning angle  $\Theta_q$  as

$$\check{\mathbf{H}}(\Theta_q) = \mathbf{a}_{RX}(\Theta_q) \mathbf{a}_{TX}^H(\Theta_q) \in \mathbb{C}^{N_R \times N_T}. \tag{8}$$

Then the equivalent echo signal of the array on this response matrix can be represented as

$$\begin{aligned}
\check{y}_{n,m}^{s,q} &= \mathbf{w}_{RX,q}^H \check{\mathbf{H}}(\Theta_q) \mathbf{x}_{q,n,m} + \check{n}_{n,m}^{s,q} \\
&= \underbrace{\sqrt{\frac{(1-\rho_q)P_t N_R}{PN_T}} \sum_{p=1}^P F_{TX}(\Theta_q, \vartheta_p) s_{n,m}^{c,p,q}}_{\text{CBE}} + \underbrace{\sqrt{\rho_q P_t N_R N_T} s_{n,m}^{s,q}}_{\text{SBE}} + \check{n}_{n,m}^{s,q}
\end{aligned} \tag{9}$$

where  $\check{n}_{n,m}^{s,q}$  is the zero-mean additive complex Gaussian white noise with variance  $\sigma_{s,q}^2$ . Note that both the communications beams echoes (CBE) and the sensing beam echoes (SBE) are beneficial for sensing and can be utilized by BS for sensing, and thus the signal-to-noise ratio (SNR) of the echo signals should be used to describe the sensing performance. Specifically, we represent the array response SNR at the sensing scanning angle  $\Theta_q$  in the  $q$ -th time slot as

$$\begin{aligned}
\text{SNR}_{s,q} &= \frac{\mathbb{E}\{|\mathbf{w}_{RX,q}^H \check{\mathbf{H}}(\Theta_q) \mathbf{x}_{q,n,m}|^2\}}{\mathbb{E}\{|\check{n}_{n,m}^{s,q}|^2\}} \\
&= \frac{(1-\rho_q)P_t N_R \sum_{p=1}^P G_{TX}(\Theta_q, \vartheta_p) + \rho_q P P_t N_R N_T}{PN_T \sigma_{s,q}^2}.
\end{aligned} \tag{10}$$

### C. Joint Communications and Sensing Power Allocation

As described in Section II. C, when the sensing scanning angle  $\Theta_q$  is located within the  $p$ -th C4S sector, BS no longer generates the dedicated sensing beam, which means that the optimal solution for  $\rho_q$  is  $\rho_q = 0$  at this time.

On the other side, when  $\Theta_q$  is located within the S4S sectors, in order to maximize system sensing performance

while ensure user communications performance, the overall optimization problem is formulated as

$$\text{(P1) : maximize } \text{SNR}_{s,q}, \tag{11}$$

$$\text{s.t. } \text{SINR}_{c,p^*,q} \geq \epsilon_{p^*}, p^* = 1, 2, \dots, P, \tag{12}$$

where  $\epsilon_{p^*}$  is the minimum SINR required for the  $p^*$ -th user. By substituting (6) into (12), the constraint (12) can be equivalently transformed into

$$\rho_q \leq \min\{\mathcal{H}_{1^*,q}, \mathcal{H}_{2^*,q}, \dots, \mathcal{H}_{P^*,q}\}, \tag{13}$$

where  $\mathcal{H}_{p^*,q}$  is defined as

$$\mathcal{H}_{p^*,q} = \frac{N_T^2 - \epsilon_{p^*} \sum_{p=1, p \neq p^*}^P G_{TX}(\vartheta_{p^*}, \vartheta_p) - \epsilon_{p^*} \frac{PN_T \sigma_{c,p^*}^2}{P_t \gamma_{p^*}^2}}{N_T^2 - \epsilon_{p^*} \sum_{p=1, p \neq p^*}^P G_{TX}(\vartheta_{p^*}, \vartheta_p) + \epsilon_{p^*} P G_{TX}(\vartheta_{p^*}, \Theta_q)}. \tag{14}$$

We then transform  $\text{SNR}_{s,q}$  into

$$\begin{aligned}
\text{SNR}_{s,q} &= \frac{P_t N_R \sum_{p=1}^P G_{TX}(\Theta_q, \vartheta_p)}{PN_T \sigma_{s,q}^2} + \\
&\quad \frac{\rho_q P_t N_R \left[ PN_T^2 - \sum_{p=1}^P G_{TX}(\Theta_q, \vartheta_p) \right]}{PN_T \sigma_{s,q}^2}.
\end{aligned} \tag{15}$$

Since  $G_{TX}(\Theta_q, \vartheta_p) \leq N_T^2$  holds for any  $p = 1, 2, \dots, P$ , there is  $PN_T^2 - \sum_{p=1}^P G_{TX}(\Theta_q, \vartheta_p) \geq 0$ . Therefore,  $\text{SNR}_{s,q}$  is a linear function of  $\rho_q$ , and increases with the increase of  $\rho_q$ . In order to maximize  $\text{SNR}_{s,q}$ , the optimal solution of  $\rho_q$  can be expressed as  $\rho_q = \min\{\mathcal{H}_{1^*,q}, \mathcal{H}_{2^*,q}, \dots, \mathcal{H}_{P^*,q}\}$ .

In all, the optimal result of  $\rho_q$  can be comprehensively expressed as

$$\rho_q = \begin{cases} \min\{\mathcal{H}_{1^*,q}, \mathcal{H}_{2^*,q}, \dots, \mathcal{H}_{P^*,q}\}, & \text{if } \Theta_q \notin (\vartheta_p - \frac{\vartheta_{3dB}^p}{2}, \vartheta_p + \frac{\vartheta_{3dB}^p}{2}) \text{ for all } p = 1, \dots, P; \\ 0, & \text{if } \Theta_q \in [\vartheta_p - \frac{\vartheta_{3dB}^p}{2}, \vartheta_p + \frac{\vartheta_{3dB}^p}{2}] \text{ for any } p = 1, \dots, P. \end{cases} \tag{16}$$

We provide some optimization details with an example in Fig. 5, in which  $N_T = 64$  antennas are configured and one user is located in  $20^\circ$  direction. Fig. 5(a) shows the optimization results of  $\rho_q$  which also represents the contribution of sensing beam to  $\text{SNR}_{s,q}$ , the contribution of communications beam to  $\text{SNR}_{s,q}$  which is represented by  $|\text{CBE}|^2$ , and the curve of  $\text{SNR}_{s,q}$  versus  $\Theta_q$ . Fig. 5(b) shows several silhouettes of transmitting beamforming, in which the blue and red lines

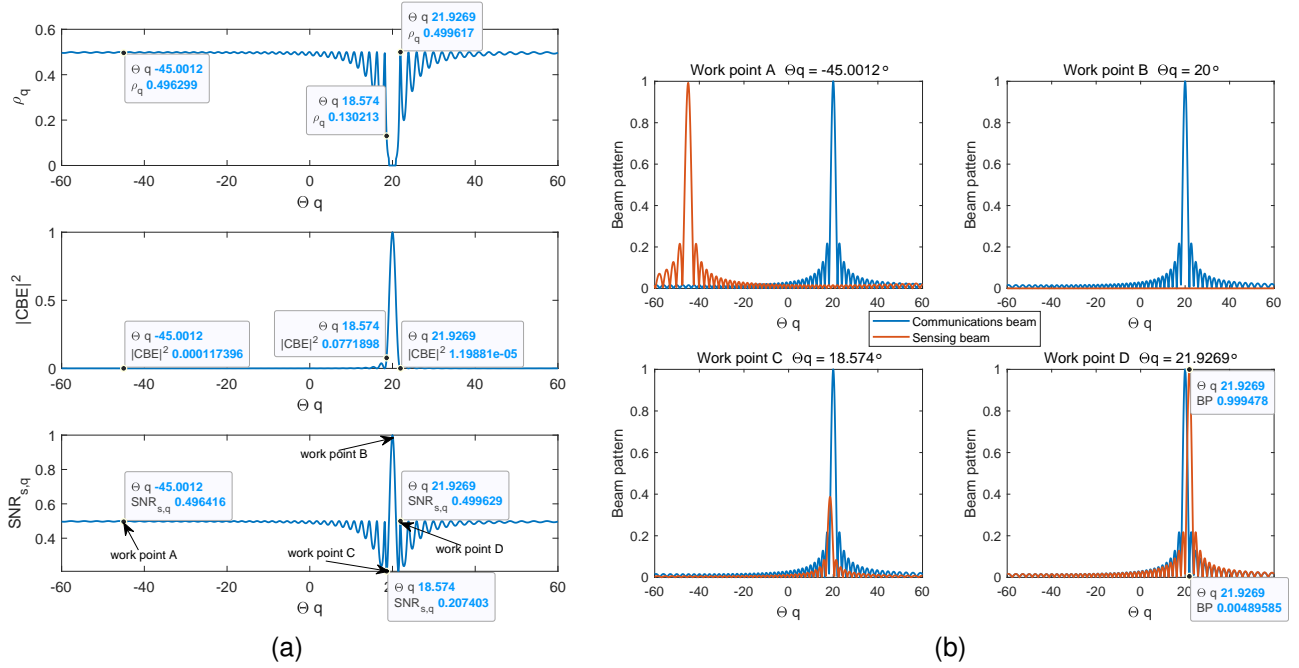


Fig. 5. (a) The examples of some optimization details; (b) Four types of work points.

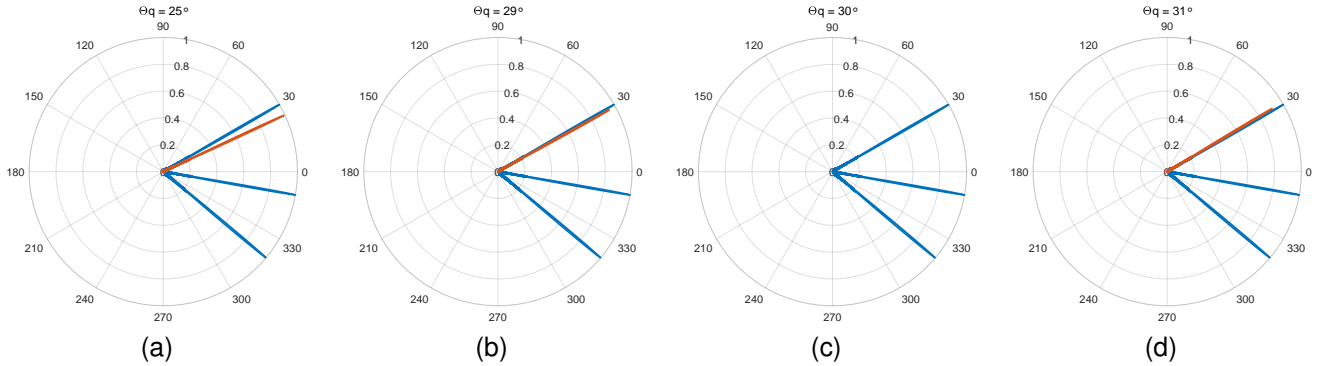


Fig. 6. (a) An example of beamforming optimization results, where  $\Theta_q$  is  $25^\circ$ . (b)  $\Theta_q = 29^\circ$ . (c)  $\Theta_q = 30^\circ$ . (d)  $\Theta_q = 31^\circ$ . Three users are located in the directions of  $-40^\circ$ ,  $-10^\circ$ , and  $30^\circ$ , respectively.

represent the communications beam and sensing beam, respectively. It is seen from Fig. 5(a) that when  $\Theta_q = -45.0012^\circ$ , due to the difference between  $\Theta_q$  and user angle, 50% of transmitting power is used to generate the sensing beam, and thus an obvious red sensing beam in  $-45.0012^\circ$  direction can be observed in the upper left part of Fig. 5(b). This situation occupies most of time during the beam scanning process, and we refer to it as working point A: *normal working point*. When  $\Theta_q = 20^\circ$  is within one C4S sector, there is  $\rho_q = 0$ , which means that BS does not allocate energy to sensing beam for ensuring the communications performance. Fortunately, it is seen from Fig. 5(a) that  $SNR_{s,q}$  actually reaches its peak value at this time, as all transmitting power is used to generate the communications beam in  $20^\circ$  direction, which can also cause target echoes to be used by BS for sensing. We refer to this situation as working point B: *peak working point*. Another noteworthy point is working point C. When  $\Theta_q = 18.574^\circ$ , due to the close between  $\Theta_q$  and user angle, to avoid excessive interference of sensing beam

on communications, the optimization result is  $\rho_q = 0.1302$ . This means that only 13.02% power is allocated to generate sensing beam, while the remaining 86.98% power is used to generate communications beam. Note that the contribution of sensing beam to  $SNR_{s,q}$  is 0.1302, while since  $\Theta_q$  is located on the sidelobe of communications beam, the contribution of communications beam to  $SNR_{s,q}$  is only 0.0772, which leads to a minimum value of  $SNR_{s,q}$  as 0.2074. We refer to these work points as *blind work points*. Furthermore, when  $\Theta_q = 21.9269^\circ$ ,  $SNR_{s,q}$  returned to the normal levels. The lower right part of Fig. 5(b) explains this phenomenon, in which the user is just at the zero point of the sensing beam, hence the sensing beam with allocated 50% power at this time will not cause serious interference to the user. We refer to this situation as working point D: *oscillating working point*.

Fig. 6 shows the examples of transmitting beamforming with multiple users, in which  $N_T = 128$  antennas are configured and three users are located in  $-40^\circ$ ,  $-10^\circ$  and  $30^\circ$ , respectively. The blue and red lines represent the com-

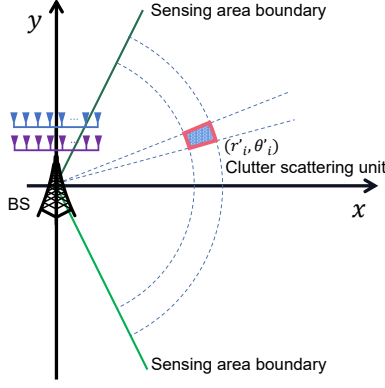


Fig. 7. Schematic diagram of static environmental clutter scattering unit.

munications beams and sensing beam, respectively. Fig. 6(a) to Fig. 6(d) show several silhouettes with  $\Theta_q$  gradually scanning from  $25^\circ$  to  $31^\circ$ , and this process undergoes a C4S sector formed by the user at  $30^\circ$  as  $[29.5452^\circ, 30.4548^\circ]$ . In Fig. 6(a), due to the difference between  $\Theta_q = 25^\circ$  and users angles, an obvious red sensing beam in  $25^\circ$  direction can be observed. In Fig. 6(c), the  $\Theta_q$  is set as  $30^\circ$ , which is within one C4S sector. Then the optimization result at this time is  $\rho_q = 0$ , which means that BS does not allocate energy to the sensing beam in order to ensure the communications performance of the user in  $30^\circ$  direction.

#### IV. DYNAMIC TARGET DETECTION AND ESTIMATION IN CLUTTER ENVIRONMENT

In this section, we will construct a practical ISAC scene with clutter environment and provide a complete and practical scheme to sense dynamic targets from clutter environment.

##### A. Echo Signals Model

As described in Section II. D, the original echo signals should include both dynamic targets echoes (DTE) and static environment echoes (SEE). Based on typical urban service scenarios, we model the clutter environment as ground clutter. Specifically, we divide the clutter area within sensing range into  $I$  static clutter scattering units based on distance and angle dimensions as the blue grid unit in Fig. 7, and the size of the clutter scattering unit is determined by the angle and distance resolution of the system. Assuming the center position of the  $i$ -th unit is  $(r'_i, \theta'_i)$ , Then the echo channel of the  $i$ -th unit on the  $m$ -th subcarrier of the  $n$ -th symbol can be modeled as

$$\mathbf{H}'_{i,n,m} = \beta_i e^{-j2\pi f_m \frac{2r'_i}{c}} \mathbf{a}_{RX}(\theta'_i) \mathbf{a}_{TX}^H(\theta'_i), \quad i = 1, \dots, I, \quad (17)$$

where  $\beta_i = \sqrt{\frac{\lambda^2}{(4\pi)^3 r_i^4}} \sigma'_{c,i}$  is the channel fading factor and  $\sigma'_{c,i}$  is the radar cross section (RCS) of the  $i$ -th clutter scattering unit. The RCS of ground clutter can usually be assumed to follow the Swerling I model, and the probability density function of RCS  $\sigma$  satisfies

$$f(\sigma) = \frac{1}{\sigma_0} \exp\left(-\frac{\sigma}{\sigma_0}\right), \sigma \geq 0, \quad (18)$$

where  $\sigma_0$  is the average value of object's RCS. Besides, the echo channel of the  $k$ -th dynamic target on the  $m$ -th subcarrier of the  $n$ -th OFDM symbol can be represented as

$$\mathbf{H}_{k,n,m} = \alpha_k e^{j2\pi f_0 \frac{2v_k n T_s}{c}} e^{-j2\pi f_m \frac{2r_k}{c}} \mathbf{a}_{RX}(\theta_k) \mathbf{a}_{TX}^H(\theta_k), \quad (19)$$

$$k = 1, \dots, K,$$

where  $n = 0, 1, 2, \dots, N-1$ ,  $\alpha_k = \sqrt{\frac{\lambda^2}{(4\pi)^3 r_k^4}} \sigma_{c,k}$ , and  $\sigma_{c,k}$  is the RCS of the  $k$ -th dynamic target that also follows Swerling I model. Based on (17) and (19), the overall sensing echoes channel matrix on the  $m$ -th subcarrier of the  $n$ -th OFDM symbol can be represented as

$$\mathbf{H}_{n,m} = \sum_{k=1}^K \mathbf{H}_{k,n,m} + \sum_{i=1}^I \mathbf{H}'_{i,n,m}. \quad (20)$$

Based on (1) and (20), the echo signal on the  $m$ -th subcarrier of the  $n$ -th OFDM symbol received by BS in the  $q$ -th time slot is

$$y_{n,m}^{s,q} = \mathbf{w}_{RX,q}^H \mathbf{H}_{n,m} \mathbf{x}_{q,n,m} + n_{n,m}^{s,q}$$

$$= \sum_{p=1}^P \mathbf{w}_{RX,q}^H \mathbf{H}_{n,m} \mathbf{w}_{c,p,q} s_{n,m}^{c,p,q} + \mathbf{w}_{RX,q}^H \mathbf{H}_{n,m} \mathbf{w}_{s,q} s_{n,m}^{s,q} + n_{n,m}^{s,q},$$

$$q = 1, \dots, Q, \quad n = 0, \dots, N-1, \quad m = 0, \dots, M-1, \quad (21)$$

where  $n_{n,m}^{s,q}$  is the zero-mean additive Gaussian noise with variance  $\sigma_{s,q}^2$ . Then we can stack  $y_{n,m}^{s,q}$  into one echoes tensor  $\mathbf{Y}_{cube} \in \mathbb{C}^{Q \times N \times M}$ , whose  $(q, n, m)$ -th element is  $\mathbf{Y}_{cube}[q, n, m] = y_{n,m}^{s,q}$ .

Note that  $\mathbf{Y}_{cube}$  includes the echoes channel, receiving and transmitting beamforming, and transmission symbols, while targets sensing can be understood as an estimation of echoes channel. However, random transmission symbols would affect the estimation of echoes channel, and thus we need to erase the transmission symbols from the received signals to obtain the equivalent echoes channel (EEC) [19]. For massive MIMO system, when  $\Theta_q$  is located within the S4S sector, it can be inferred from (21) that  $y_{n,m}^{s,q} \approx \mathbf{w}_{RX,q}^H \mathbf{H}_{n,m} \mathbf{w}_{s,q} s_{n,m}^{s,q} + n_{n,m}^{s,q}$ , which means that the sensing echoes are mainly provided by the sensing beam at this time, and thus the EEC corresponding to  $y_{n,m}^{s,q}$  can be obtained as  $\tilde{h}_{n,m}^{s,q} = y_{n,m}^{s,q} / s_{n,m}^{s,q}$ . When  $\Theta_q$  is located within the  $p$ -th C4S sector, it can be inferred from (21) that  $y_{n,m}^{s,q} \approx \mathbf{w}_{RX,q}^H \mathbf{H}_{n,m} \mathbf{w}_{c,p,q} s_{n,m}^{c,p,q} + n_{n,m}^{s,q}$ , which means that the sensing echoes are mainly provided by the  $p$ -th communications beam at this time, and thus the EEC corresponding to  $y_{n,m}^{s,q}$  can be obtained as  $\tilde{h}_{n,m}^{s,q} = y_{n,m}^{s,q} / s_{n,m}^{c,p,q}$ . Then we can comprehensively define the EEC as  $\tilde{h}_{n,m}^{s,q} = y_{n,m}^{s,q} / s_{n,m}^{t,q}$ , where  $s_{n,m}^{t,q}$  is designed as

$$s_{n,m}^{t,q} = \begin{cases} s_{n,m}^{s,q}, & \text{if } \Theta_q \notin (\vartheta_p - \frac{\vartheta_{3dB}}{2}, \vartheta_p + \frac{\vartheta_{3dB}}{2}) \text{ for all } p = 1, \dots, P; \\ s_{n,m}^{c,p,q}, & \text{if } \Theta_q \in [\vartheta_p - \frac{\vartheta_{3dB}}{2}, \vartheta_p + \frac{\vartheta_{3dB}}{2}] \text{ for any } p = 1, \dots, P. \end{cases} \quad (22)$$

Besides, we can stack  $\tilde{h}_{n,m}^{s,q}$  into an EEC tensor  $\tilde{\mathbf{H}}_{cube} \in \mathbb{C}^{Q \times N \times M}$ , with  $\tilde{\mathbf{H}}_{cube}[q, n, m] = \tilde{h}_{n,m}^{s,q}$ .

### B. Static Environmental Clutter Filtering Based on Mean Phasor Cancellation

It can be analyzed from (20) and (21) that the echo signals  $\mathbf{Y}_{cube}$  includes both DTE and SEE, and the corresponding EEC  $\tilde{\mathbf{H}}_{cube}$  also includes both the EEC of dynamic targets (DT-EEC) and the EEC of static environment (SE-EEC). As introduced in Section I, the sensing tasks of ISAC system can be divided into SES and DTS, while DTS can be considered as an estimation of DT-EEC. However, when we focus on DTS problem, the SE-EEC in the original echo signals would cause negative interference to DTS, and thus SE-EEC can be referred to as the clutter-EEC. To address this negative interference, we need to filter out the interference of clutter-EEC (SE-EEC) and to extract the effective DT-EEC from  $\tilde{\mathbf{H}}_{cube}$ .

To begin with, the EEC of the  $m$ -th subcarrier in  $\tilde{\mathbf{H}}_{cube}$  is  $\tilde{\mathbf{H}}_m^M = \tilde{\mathbf{H}}_{cube}[:, :, m] \in \mathbb{C}^{Q \times N}$ , i.e.,

$$\tilde{\mathbf{H}}_m^M = \begin{bmatrix} \mathbf{w}_{RX,1}^H \mathbf{H}_{0,m} \tilde{\mathbf{x}}_{1,0,m} & \cdots & \mathbf{w}_{RX,1}^H \mathbf{H}_{N-1,m} \tilde{\mathbf{x}}_{1,N-1,m} \\ \vdots & \ddots & \vdots \\ \mathbf{w}_{RX,Q}^H \mathbf{H}_{0,m} \tilde{\mathbf{x}}_{Q,0,m} & \cdots & \mathbf{w}_{RX,Q}^H \mathbf{H}_{N-1,m} \tilde{\mathbf{x}}_{Q,N-1,m} \end{bmatrix} + \mathbf{N}_m^M \quad (23)$$

where  $\tilde{\mathbf{x}}_{q,n,m} = \mathbf{x}_{q,n,m}/s_{n,m}^{t,q}$ , and the  $(q, n)$ -th element in  $\mathbf{N}_m^M$  is  $\mathbf{N}_m^M[q, n] = n_{n,m}^{s,q}/s_{n,m}^{t,q}$ . Next, considering that the phase of SE-EEC remains unchanged within multiple OFDM symbols while the phase of DT-EEC changes with the target velocity within multiple OFDM symbols, we may average each row of  $\tilde{\mathbf{H}}_m^M$  and obtain the equivalent echoes channel vector caused by static environment as  $\tilde{\mathbf{h}}_m^{static} \in \mathbb{C}^{Q \times 1}$ , whose  $q$ -th element is  $\tilde{h}_m^{static}[q] = \frac{1}{N} \sum_{n=0}^{N-1} \tilde{y}_{n,m}^{s,q} = \frac{1}{N} \sum_{n=0}^{N-1} (\mathbf{w}_{RX,q}^H \mathbf{H}_{n,m} \mathbf{x}_{q,n,m}/s_{n,m}^{t,q} + n_{n,m}^{s,q}/s_{n,m}^{t,q})$ . Note that  $\tilde{\mathbf{h}}_m^{static}$  can be used to reconstruct the SE-EEC as  $\tilde{\mathbf{H}}_m^{static} = [\tilde{h}_m^{static}, \dots, \tilde{h}_m^{static}] \in \mathbb{C}^{Q \times N}$ . Then the DT-EEC of the  $m$ -th subcarrier can be extracted as  $\tilde{\mathbf{H}}_m^{dynamic} = \tilde{\mathbf{H}}_m^M - \tilde{\mathbf{H}}_m^{static}$ , and we represent the  $(q, n)$ -th element in  $\tilde{\mathbf{H}}_m^{dynamic}$  as

$$\tilde{h}_{q,n,m} = \mathbf{w}_{RX,q}^H \left( \sum_{k=1}^K \mathbf{H}_{k,n,m} \right) \tilde{\mathbf{x}}_{q,n,m} - \underbrace{\frac{1}{N} \sum_{n=0}^{N-1} \left[ \mathbf{w}_{RX,q}^H \left( \sum_{k=1}^K \mathbf{H}_{k,n,m} \right) \tilde{\mathbf{x}}_{q,n,m} \right]}_{\mathcal{I}'_{q,n,m}} + \tilde{n}_{n,m}^{s,q} \quad (24)$$

where  $\mathcal{I}'_{q,n,m}$  is defined as the remaining term after clutter filtering, and  $\tilde{n}_{n,m}^{s,q} = n_{n,m}^{s,q}/s_{n,m}^{t,q} - \frac{1}{N} \sum_{n=0}^{N-1} n_{n,m}^{s,q}/s_{n,m}^{t,q}$ . Because the Doppler term in DT-EEC varies linearly with continuous symbols, it is easy to prove that  $\lim_{N \rightarrow \infty} \mathcal{I}'_{q,n,m} = 0$ . We name the static environmental clutter filtering method as the mean phasor cancellation (MPC) method.

After filtering out the static environmental clutter, the  $\tilde{h}_{q,n,m}$  in (24) can be rewritten as (25) at the bottom of this page, where  $e^{j\phi_{n,m}^{k,q}} = e^{j\frac{4\pi f_0 v_k n T_s}{c}} e^{-j\frac{4\pi f_m r_k}{c}}$ , and  $F_{RX}(\theta_1, \theta_2) \triangleq \mathbf{a}_{RX}^H(\theta_1) \mathbf{a}_{RX}(\theta_2)$ . Considering the randomness of dynamic target distribution, we assume that there are  $K_q$  dynamic targets simultaneously in the direction  $\Theta_q$  with  $\sum_{q=1}^Q K_q = K$ . For massive MIMO systems with  $N_T \rightarrow \infty$  and  $N_R \rightarrow \infty$ ,  $\tilde{h}_{q,n,m}$  can be further calculated as (26) at the bottom of this page. Then the  $\tilde{h}_{q,n,m}$  on all subcarriers of all OFDM symbols in all time slots can be stacked into a DT-EEC tensor  $\tilde{\mathbf{H}}_{cube}^{dynamic} \in \mathbb{C}^{Q \times N \times M}$ , whose  $(q, n, m)$ -th element is  $\tilde{\mathbf{H}}_{cube}^{dynamic}[q, n, m] = \tilde{h}_{q,n,m}$ .

### C. Dynamic Targets Detection and Angle Estimation

In order to detect the presence of dynamic targets from  $\tilde{\mathbf{H}}_{cube}^{dynamic}$ , we extract the DT-EEC of the  $m$ -th subcarrier from  $\tilde{\mathbf{H}}_{cube}^{dynamic}$  as  $\tilde{\mathbf{H}}_m^{dynamic} = \tilde{\mathbf{H}}_{cube}^{dynamic}[:, :, m] \in \mathbb{C}^{Q \times N}$ . Next, considering that the sensing scanning angle dimension in  $\tilde{\mathbf{H}}_m^{dynamic}$  contains angle information of dynamic targets while the OFDM symbol dimension contains velocity information of dynamic targets, we perform an  $N$ -point fast Fourier transform (FFT) on each row of  $\tilde{\mathbf{H}}_m^{dynamic}$ , and move the zero-frequency component of the transformed spectrum to the center of the array [32], [33]. By doing so, we can obtain the angle-Doppler spectrum for DT-EEC of the  $m$ -th subcarrier as

$$\tilde{\mathbf{H}}_m^{AD} = \text{FFTshift}\{\text{FFT}\{\tilde{\mathbf{H}}_m^{dynamic}, N, 2\}, N, 2\}. \quad (27)$$

For clarity, we introduce a corresponding matrix  $\tilde{\mathbf{G}}_m^{AD}$  for  $\tilde{\mathbf{H}}_m^{AD}$ , which satisfies  $\tilde{\mathbf{G}}_m^{AD}[q, n] = |\tilde{\mathbf{H}}_m^{AD}[q, n]|$ . It can be analyzed from (26) that when the resolutions of angle and velocity are sufficient, there will be  $K$  peaks in  $\tilde{\mathbf{G}}_m^{AD}$ , which correspond to  $K$  dynamic targets one by one.

To further overcome the impact of noise and other factors, it is necessary to set appropriate local thresholds to detect each target from  $\tilde{\mathbf{G}}_m^{AD}$ , which is referred to as *radar target detection*. Constant threshold (CT) detector and constant false alarm rate (CFAR) detector are two main methods for target

$$\tilde{h}_{q,n,m} = \tilde{\mathbf{H}}_m^{dynamic}[q, n] \approx \mathbf{w}_{RX,q}^H \left( \sum_{k=1}^K \mathbf{H}_{k,n,m} \right) \tilde{\mathbf{x}}_{q,n,m} + \tilde{n}_{n,m}^{s,q} \quad (25)$$

$$= \sum_{k=1}^K \left\{ \frac{\alpha_k e^{j\phi_{n,m}^{k,q}}}{\sqrt{N_R}} F_{RX}(\Theta_q, \theta_k) \left[ \sum_{p=1}^P \sqrt{\frac{(1-\rho_q) P_t}{P N_T}} F_{TX}(\theta_k, \vartheta_p) \frac{s_{n,m}^{c,p,q}}{s_{n,m}^{t,q}} + \sqrt{\frac{\rho_q P_t}{N_T}} F_{TX}(\theta_k, \Theta_q) \frac{s_{n,m}^{s,q}}{s_{n,m}^{t,q}} \right] \right\} + \tilde{n}_{n,m}^{s,q}$$

$$\tilde{h}_{q,n,m} \approx \begin{cases} \tilde{n}_{n,m}^{s,q}, & \text{if } \Theta_q \neq \theta_k \text{ for all } k = 1, \dots, K, \\ \sum_{k'=1}^{K_q} \alpha_{k'} e^{j\phi_{n,m}^{k',q}} \sqrt{\frac{\rho_q P_t N_T N_R}{P}} + \tilde{n}_{n,m}^{s,q}, & \text{if } \Theta_q = \theta_k \neq \vartheta_p \text{ for part of } k \text{ and for all } p = 1, \dots, P, \\ \sum_{k'=1}^{K_q} \alpha_{k'} e^{j\phi_{n,m}^{k',q}} \sqrt{\frac{1-\rho_q}{P} P_t N_T N_R} + \tilde{n}_{n,m}^{s,q}, & \text{if } \Theta_q = \theta_k = \vartheta_p \text{ for part of } k \text{ and any } p = 1, \dots, P. \end{cases} \quad (26)$$



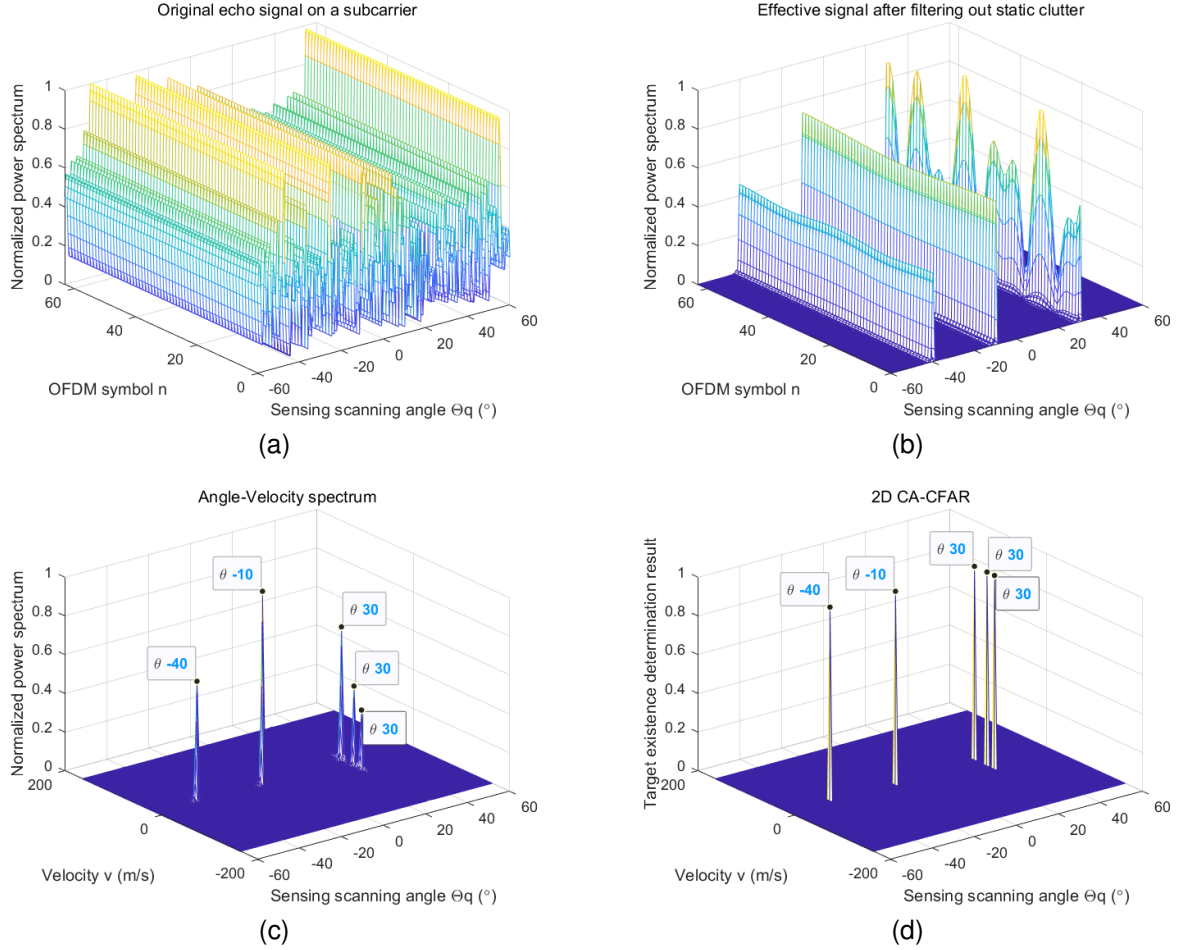


Fig. 8. (a) The power spectrum of the original echo signals on a certain subcarrier. (b) Signal power spectrum after filtering out static environmental clutter. (c) The angle-Doppler spectrum. (d) The detection results of MSJD. The five dynamic targets are set as  $(100m, -40^\circ, 10m/s)$ ,  $(60m, -10^\circ, 5m/s)$ ,  $(90m, 30^\circ, 15m/s)$ ,  $(150m, 30^\circ, -10m/s)$  and  $(200m, 30^\circ, -25m/s)$ .

detection [34]. Here, we propose a joint detection method over multiple subcarriers (MSJD) based on CFAR and CT detectors, which can be divided into the following two steps: 1) We take  $\tilde{\mathbf{G}}_m^{AD}$  as the input, set appropriate reference range and protection range, and perform two-dimensional cell-averaging CFAR (2D-CA-CFAR) detection on  $\tilde{\mathbf{G}}_m^{AD}$ . Then we can obtain the judgment matrix over single subcarrier  $\mathbf{G}_m^{out}$  as the output. 2) We compute  $\mathbf{G}_m^{out}$  for each subcarrier, and accumulate them together to obtain  $\mathbf{G}^{out} = \sum_{m=1}^M \mathbf{G}_m^{out}$ . Next we set a fixed threshold and perform CT detection on  $\mathbf{G}^{out}$  to obtain the judgment matrix over multiple subcarriers as  $\mathbf{G}_{mask}^{out}$ . Then we can detect each target from  $\mathbf{G}_{mask}^{out}$ , and the accurate angle estimation results for each dynamic target can also be obtained from  $\mathbf{G}_{mask}^{out}$  as  $\{\hat{\theta}_1, \hat{\theta}_2, \dots, \hat{\theta}_K\}$ .

Fig. 8 shows examples of clutter filtering, angle-Doppler spectrum estimation (ADSE) and MSJD under noiseless conditions, where five dynamic targets are set as  $(100m, -40^\circ, 10m/s)$ ,  $(60m, -10^\circ, 5m/s)$ ,  $(90m, 30^\circ, 15m/s)$ ,  $(150m, 30^\circ, -10m/s)$  and  $(200m, 30^\circ, -25m/s)$ . It is seen from Fig. 8(a) that the original echo signals carry dense clutter caused by static environment. After MPC cancellation, Fig. 8(b) only retains the effective echoes caused by dynamic targets. After

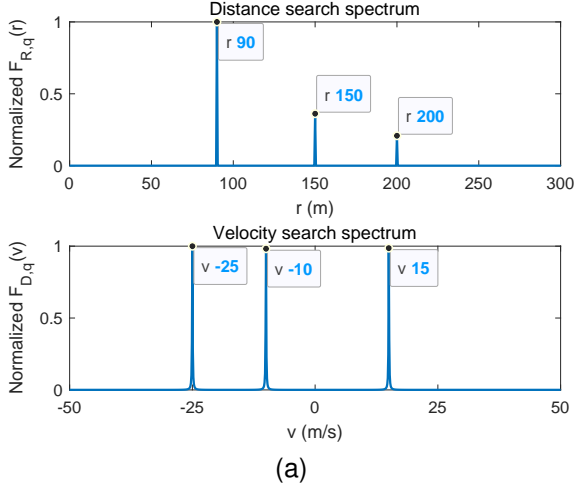
performing velocity FFT on the complex signals, five peaks corresponding to five dynamic targets can be clearly observed in the angle-Doppler spectrum shown in Fig. 8(c), which can also be observed in the MSJD results shown in Fig. 8(d). Then the angle estimates of the dynamic targets can be obtained as  $-40^\circ, -10^\circ, 30^\circ, 30^\circ$  and  $30^\circ$ , respectively.

#### D. Distance and Velocity Estimation for Dynamic Targets

After obtaining the angle estimates, we may suppose that  $K_q$  detected targets are located in the same angle  $\Theta_q$ , and represent the parameters of the  $k'_q$ -th dynamic target as  $(r_{k'_q}, \Theta_q, v_{k'_q})$ , where  $k'_q = 1, 2, \dots, K_q$ . Then the DT-EEC of this beam scanning angle within all subcarriers and symbols can be represented as  $\tilde{\mathbf{H}}_q^{RD} \in \mathbb{C}^{N \times M}$ , whose  $(n, m)$ -th element is  $\tilde{\mathbf{H}}_q^{RD}[n, m] = h_{q,n,m}$ . Based on (26),  $\tilde{\mathbf{H}}_q^{RD}$  and its transpose matrix  $(\tilde{\mathbf{H}}_q^{RD})^T$  can be respectively represented as

$$\tilde{\mathbf{H}}_q^{RD} = \zeta_q \sum_{k'_q=1}^{K_q} \alpha'_{k'_q} \mathbf{k}_D(v_{k'_q}) \mathbf{k}_R^T(r_{k'_q}) + \mathbf{N}_q^{RD}, \quad (28)$$

$$(\tilde{\mathbf{H}}_q^{RD})^T = \zeta_q \sum_{k'_q=1}^{K_q} \alpha'_{k'_q} \mathbf{k}_R(r_{k'_q}) \mathbf{k}_D^T(v_{k'_q}) + (\mathbf{N}_q^{RD})^T, \quad (29)$$



### Distance-Velocity Matching

$$\check{r}_1 = 90m, \check{r}_2 = 150m, \check{r}_3 = 200m$$

$$\check{v}_1 = -25m/s, \check{v}_2 = -10m/s, \check{v}_3 = 15m/s$$

### Results after matching

$$(\hat{r}_{30^\circ,1}, \hat{v}_{30^\circ,1}) = (\check{r}_1, \check{v}_3) = (90m, 15m/s)$$

$$(\hat{r}_{30^\circ,2}, \hat{v}_{30^\circ,2}) = (\check{r}_2, \check{v}_2) = (150m, -10m/s)$$

$$(\hat{r}_{30^\circ,3}, \hat{v}_{30^\circ,3}) = (\check{r}_3, \check{v}_1) = (200m, -25m/s)$$

$\check{r}_i$	$\check{v}_j$	Normalized $S_q(\check{r}_i, \check{v}_j)$
$\check{r}_1$	$\check{v}_1$	0.022
$\check{r}_1$	$\check{v}_2$	0.021
$\check{r}_1$	$\check{v}_3$	1.000
$\check{r}_2$	$\check{v}_1$	0.021
$\check{r}_2$	$\check{v}_2$	0.600
$\check{r}_2$	$\check{v}_3$	0.014
$\check{r}_3$	$\check{v}_1$	0.450
$\check{r}_3$	$\check{v}_2$	0.020
$\check{r}_3$	$\check{v}_3$	0.009

Fig. 9. (a) An example of velocity estimation based on searching  $F_{D,q}(v)$ ; (b) An example of distance estimation based on searching  $F_{R,q}(r)$ . Three dynamic targets are set as  $(90m, 30^\circ, 15m/s)$ ,  $(150m, 30^\circ, -10m/s)$  and  $(200m, 30^\circ, -25m/s)$ .

where  $\zeta_q$  is the amplitude term,  $\alpha'_{k'_q} = \alpha_{k'_q} e^{-j \frac{4\pi f_0 r_{k'_q}}{c}}$ ,  $\mathbf{N}_q^{RD}$  is the corresponding noise matrix,  $\mathbf{k}_D(v) = [1, e^{j \frac{4\pi f_0 v T_s}{c}}, \dots, e^{j \frac{4\pi f_0 v T_s (N-1)}{c}}]^T \in \mathbb{C}^{N \times 1}$  is defined as the *Doppler array steering vector*, and  $\mathbf{k}_R(r) = [1, e^{-j \frac{4\pi r \Delta f}{c}}, \dots, e^{-j \frac{4\pi r \Delta f (M-1)}{c}}]^T \in \mathbb{C}^{M \times 1}$  is defined as the *distance array steering vector*. From (28) and (29), it can be seen that  $\tilde{\mathbf{H}}_q^{RD}$  and  $(\tilde{\mathbf{H}}_q^{RD})^T$  are the generalized array signals related to Doppler array and distance array, respectively. To estimate the velocity and distance of dynamic targets, the autocorrelation matrices of  $\tilde{\mathbf{H}}_q^{RD}$  and  $(\tilde{\mathbf{H}}_q^{RD})^T$  are calculated as  $\mathbf{R}_{D,q}^X = \frac{1}{M} \tilde{\mathbf{H}}_q^{RD} (\tilde{\mathbf{H}}_q^{RD})^H$  and  $\mathbf{R}_{R,q}^X = \frac{1}{N} (\tilde{\mathbf{H}}_q^{RD})^T ((\tilde{\mathbf{H}}_q^{RD})^T)^H$ . We perform eigenvalue decomposition of  $\mathbf{R}_{D,q}^X$  and  $\mathbf{R}_{R,q}^X$  to obtain the diagonal matrix with eigenvalues ranging from large to small ( $\Sigma_{D,q}$  and  $\Sigma_{R,q}$ ) and the corresponding eigenvector matrix ( $\mathbf{U}_{D,q}$  and  $\mathbf{U}_{R,q}$ ). That is  $[\mathbf{U}_{D,q}, \Sigma_{D,q}] = \text{eig}(\mathbf{R}_{D,q}^X)$  and  $[\mathbf{U}_{R,q}, \Sigma_{R,q}] = \text{eig}(\mathbf{R}_{R,q}^X)$ . Then the minimum description length (MDL) criterion is utilized to estimate the number of dynamic targets from  $\Sigma_{D,q}$  and  $\Sigma_{R,q}$  as  $K_{q,D}^{MDL}$  and  $K_{q,R}^{MDL}$  respectively [35], [36], and we define  $K_q^{MDL} = \min\{K_{q,D}^{MDL}, K_{q,R}^{MDL}\}$  as the number of dynamic targets to be estimated from  $\mathbf{H}_q^{RD}$ . Therefore, the noise space related to the Doppler array can be represented as  $\mathbf{U}_{D,q}^N = \mathbf{U}_{D,q}[:, K_q^{MDL} + 1 : N]$ , and the noise space related to the distance array can be represented as  $\mathbf{U}_{R,q}^N = \mathbf{U}_{R,q}[:, K_q^{MDL} + 1 : M]$ . Then the Doppler spectral function with search velocity  $v$  and the distance spectral function with search distance  $r$  can be defined as

$$F_{D,q}(v) = \frac{1}{\mathbf{k}_D^H(v) \mathbf{U}_{D,q}^N (\mathbf{U}_{D,q}^N)^H \mathbf{k}_D(v)}, \quad (30)$$

$$F_{R,q}(r) = \frac{1}{\mathbf{k}_R^H(r) \mathbf{U}_{R,q}^N (\mathbf{U}_{R,q}^N)^H \mathbf{k}_R(r)}. \quad (31)$$

By searching for the peaks of  $F_{D,q}(v)$  and  $F_{R,q}(r)$ , we can obtain the preliminary velocity estimates for  $K_q$  targets as  $\{\check{v}_1, \check{v}_2, \dots, \check{v}_{K_q}\}$  and the preliminary distance estimates for  $K_q$  targets as  $\{\check{r}_1, \check{r}_2, \dots, \check{r}_{K_q}\}$ , respectively. Next, in order

to obtain the unique parameters information for each target from the preliminary estimates, we must realize distance and velocity matching from  $\{\check{v}_1, \check{v}_2, \dots, \check{v}_{K_q}\}$  and  $\{\check{r}_1, \check{r}_2, \dots, \check{r}_{K_q}\}$ . Specifically, we construct a distance-velocity set as  $\Xi_q = \{(\check{r}_1, \check{v}_1), \dots, (\check{r}_1, \check{v}_{K_q}), \dots, (\check{r}_{K_q}, \check{v}_1), \dots, (\check{r}_{K_q}, \check{v}_{K_q})\}$  containing  $K_q^2$  elements. Then the matching value of the element  $(r_i, v_j)$  in  $\Xi_q$  can be calculated as

$$S_q(r_i, v_j) = |\mathbf{k}_D^H(v_j) \mathbf{H}_q^{RD} \mathbf{k}_R^*(r_i)|. \quad (32)$$

After performing (32) for all  $r_i$  and  $v_j$  pairs, the set of matching values corresponding to the set  $\Xi_q$  can be represented as  $\Xi_q^S$ . By searching for the  $K_q$  elements with the highest value in  $\Xi_q^S$  and their corresponding elements in  $\Xi_q$ , we can estimate the distances and velocities of these  $K_q$  dynamic targets as  $\{(\hat{r}_{q,1}, \hat{v}_{q,1}), (\hat{r}_{q,2}, \hat{v}_{q,2}), \dots, (\hat{r}_{q,K_q}, \hat{v}_{q,K_q})\}$ .

Fig. 9 shows examples of distance and velocity estimation and distance-velocity matching under noiseless conditions, for estimation of three targets located in  $30^\circ$  direction set in Fig. 8. The preliminary distance can be estimated from the distance search spectrum in Fig. 9(a) as  $90m$ ,  $150m$  and  $200m$ , while the preliminary velocity can be estimated from the velocity search spectrum as  $-25m/s$ ,  $-10m/s$  and  $15m/s$ . Fig. 9(b) shows the process of distance-velocity matching using (32), and we can obtain the estimation results for the three dynamic targets located in  $30^\circ$  direction, which are  $(90m, 30^\circ, 15m/s)$ ,  $(150m, 30^\circ, -10m/s)$  and  $(200m, 30^\circ, -25m/s)$ .

## V. SIMULATION RESULTS

In simulations, we set the number of antennas for transmitting array as  $N_T = 128$ , the number of antennas for receiving array as  $N_R = 128$ , the lowest carrier frequency as  $f_0 = 220$  GHz and the antenna spacing as  $d = \frac{1}{2}\lambda$ . Assume that the required sensing range of the BS is  $[\theta_{start}, \theta_{end}] = [60^\circ, -60^\circ]$ . The noise is assumed to obey the complex Gaussian distribution with mean  $\mu = 0$  and variance  $\sigma_n^2 = 1$ . The root mean square error (RMSE) of angle estimation, distance estimation, and velocity estimation are defined as  $\text{RMSE}_\theta =$

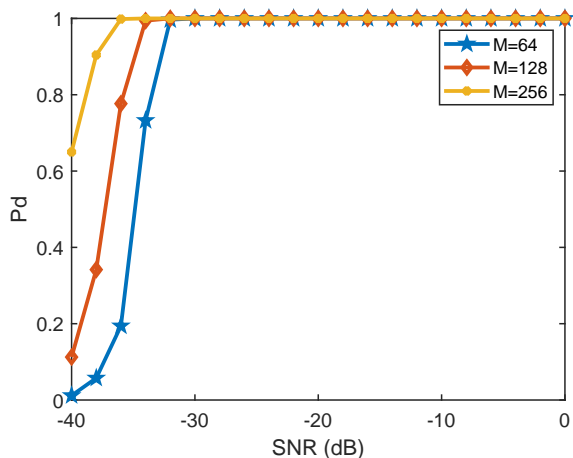


Fig. 10. Curve of dynamic target detection probability versus SNR.

$\sqrt{\frac{\sum_{i=1}^{Count} (\hat{\theta}_{s(i)} - \theta_s)^2}{Count}}$ ,  $RMSE_r = \sqrt{\frac{\sum_{i=1}^{Count} (\hat{r}_{s(i)} - r_s)^2}{Count}}$  and  $RMSE_v = \sqrt{\frac{\sum_{i=1}^{Count} (\hat{v}_{s(i)} - v_s)^2}{Count}}$ , where *Count* is the number of the Monte Carlo runs, the real parameters of the dynamic target is  $(r_s, \theta_s, v_s)$ , and  $(\hat{r}_{s(i)}, \hat{\theta}_{s(i)}, \hat{v}_{s(i)})$  is the estimation parameters of the target.

It is worth pointing out that existing ISAC schemes [15]–[19] that do not consider clutter environment cannot detect the targets and estimate their parameters in actual clutter environment as shown in Fig. 8(a). Thus, we did not show the performance of the existing methods in the simulations.

#### A. Performance of Dynamic Target Detection

We set that the subcarrier frequency interval is  $\Delta f = 200$  kHz, and the number of OFDM symbols is  $N = 64$ . Fig. 10 shows the performance curve of dynamic target detection probability  $P_d$  over multiple subcarriers with different subcarrier numbers. It can be seen that  $P_d$  gradually increases with the increase of SNR. When the SNR is greater than a certain value,  $P_d$  can almost approach 100%. In addition, when the SNR is low,  $P_d$  increases with the increase of  $M$ , which verifies the effectiveness of the proposed joint detection method over multiple subcarriers.

#### B. Performance of Dynamic Target Parameter Estimation

We assume that the subcarrier frequency interval is  $\Delta f = 500$  kHz, the number of OFDM symbols is  $N = 64$ , and the number of subcarriers is  $M = 128$ . Fig. 11 shows the curves of sensing RMSE versus SNR for different dynamic targets.

It can be seen from Fig. 11(a) that the  $RMSE_\theta$  gradually decreases with the increase of SNR. When the SNR is less than  $-25$  dB, the  $RMSE_\theta$  is large and there is no significant change for  $RMSE_\theta$  with the change of SNR. As the SNR increases from  $-25$  dB to  $-10$  dB, the  $RMSE_\theta$  rapidly decreases from  $0.15^\circ$  to  $0.01^\circ$ . As the SNR further increases, the  $RMSE_\theta$  continues to decrease. In addition, when the distance and velocity parameters are fixed, the closer the angle of the dynamic target approaches  $0^\circ$ , the smaller its  $RMSE_\theta$  will be. This is mainly because the beam generated by antenna array is narrower near  $0^\circ$ , which improves the performance of angle sensing to some extent.

Fig. 11(b) shows the variation curve of  $RMSE_r$  versus SNR, where three dynamic targets are fixed in  $20^\circ$  direction, but their distances are different. It can be seen that when the SNR is low, the  $RMSE_r$  remains at a large value, which means that it is difficult to estimate the target parameters under harsh SNR conditions. Nevertheless, when the SNR is greater than 0 dB, the proposed sensing scheme can accurately estimate the distance of the three targets.

Fig. 11(c) shows the RMSE variation curve of target velocity sensing versus SNR. For the target at  $50m$ , when the SNR reaches  $-10$  dB, its velocity sensing RMSE is about  $0.1m/s$ . When the SNR increases to 10 dB, the  $RMSE_v$  decreases to  $0.01m/s$ , which indicates that the proposed sensing scheme has high velocity sensing accuracy.

By comparing the sensing results of three targets at different distances in Fig. 11(b) and Fig. 11(c), we can find that the sensing error of targets at farther distances is larger. This is mainly because the signal power of the dynamic target echo decreases with the increase of target distance, and thus, farther targets will be more susceptible to noise.

#### C. The Impact of System Resolution on Sensing Performance

The sensing accuracy of a system is usually related to its sensing resolution. Here we will explore the impact of system parameters on sensing resolution and performance.

Fig. 12(a) shows the variation of RMSE versus SNR for angle sensing under different array sizes, in which the subcarrier frequency interval is  $\Delta f = 500$  kHz, the number of symbols is  $N = 32$  and the number of subcarriers is  $M = 128$ . It is seen that when the number of transmitting array antennas  $N_T$  or the number of receiving array antennas  $N_R$  is fixed, the accuracy of angle sensing gradually improves with the increase of  $N_R$  or  $N_T$ . This phenomenon is mainly because the angle resolution of MIMO systems is inversely proportional to the number of antennas, and more antennas can form narrower beams to provide higher sensing performance.

Fig. 12(b) shows the variation of RMSE versus SNR for distance sensing under different numbers of subcarriers, in which the array size are  $N_T = 128$  and  $N_R = 128$ , subcarrier frequency interval is  $\Delta f = 500$  kHz, and the number of OFDM symbols is  $N = 32$ . It can be seen from the figure that the RMSE of distance sensing significantly decreases with the increase of the number of subcarriers  $M$ . In fact, when  $\Delta f$  is fixed, the system transmission bandwidth  $W = (M - 1)\Delta f$  linearly increases with  $M$ , and the distance resolution  $\Delta r = \frac{c}{2B} = \frac{c}{2(M-1)\Delta f}$  gradually decreases in numerical value [37]. Hence, more subcarriers can realize higher distance resolution, which in turn leads to higher distance sensing accuracy.

Fig. 12(c) shows the variation of RMSE versus SNR for velocity sensing under different numbers of OFDM symbols, in which the array size are  $N_T = 128$  and  $N_R = 128$ , subcarrier frequency interval is  $\Delta f = 500$  kHz, and the number of subcarriers is  $M = 128$ . It can be observed that when  $N$  is not very large, the accuracy of velocity sensing is already quite satisfactory. In addition, the RMSE of velocity sensing decreases significantly with the increase of  $N$ . In reality, when  $\Delta f$  is fixed, the velocity resolution of the system  $\Delta v = \frac{c}{2f_0 N T_s}$  decreases as  $N$  increases [37]. Hence,

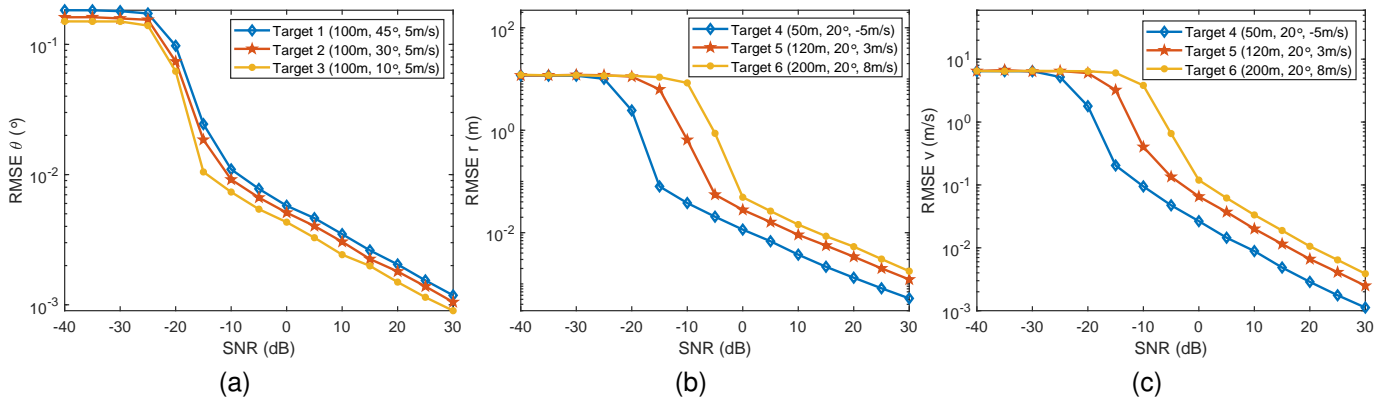


Fig. 11. (a) The RMSE of dynamic target angle sensing; (b) The RMSE of dynamic target distance sensing; (c) The RMSE of dynamic target velocity sensing.

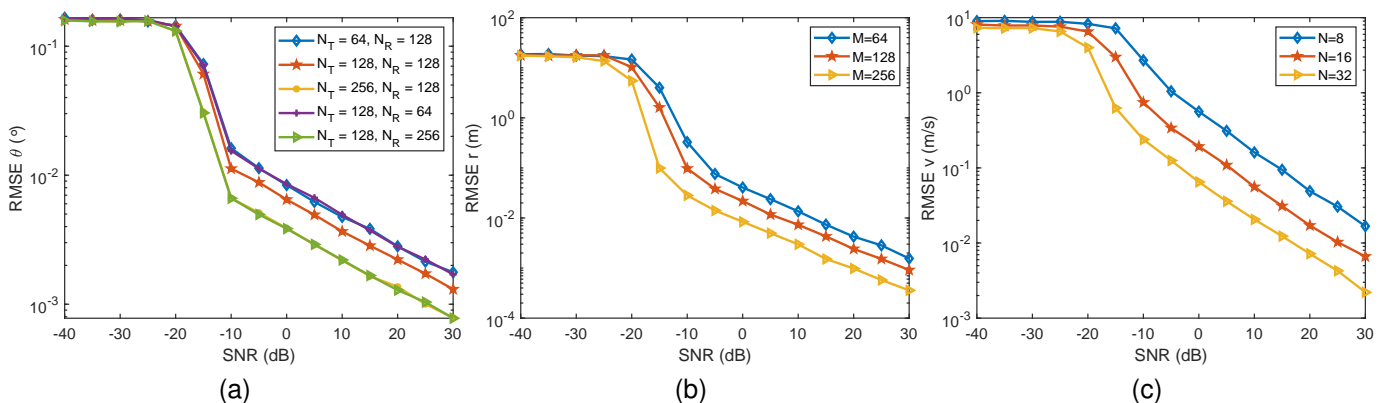


Fig. 12. (a) The RMSE for angle sensing under different array sizes; (b) The RMSE for distance sensing under different numbers of subcarriers; (c) The RMSE for velocity sensing under different numbers of OFDM symbols.

more OFDM symbols can bring higher velocity resolution and achieve higher accuracy in velocity sensing.

#### D. Communications Performance Evaluation

In this subsection, we will evaluate the communications performance of the proposed ISAC process by using the bit error rate (BER) as the indicator. We set three communication users located in the  $-40^\circ$ ,  $0^\circ$ , and  $30^\circ$  directions. One sensing beam scans the entire space, and three communications beams communicate with the users for data transmission, in which 16-QAM is employed for communications signals modulation. The number of subcarriers is set to  $M = 512$ , the subcarrier frequency interval is set to  $\Delta f = 480$  kHz, the number of OFDM symbols is set to  $N = 64$ , and the number of BS transmitting antennas  $N_T$  is set as a variable.

Fig. 13 shows the curve of BER versus SINR under different array sizes. It can be seen that when the SINR of the user is high enough, BER gradually decreases as the SINR increases. However, when  $N_T$  is small, BER will converge to an error floor as SINR increases. This is mainly because when the antenna array is small, it is difficult to alleviate inter users interference and sensing interference to communications. In addition, it can be found that BER gradually decreases as  $N_T$  increases. When  $N_T$  is 256 and SINR is 40 dB, the overall BER of communication in the simulation is almost zero.

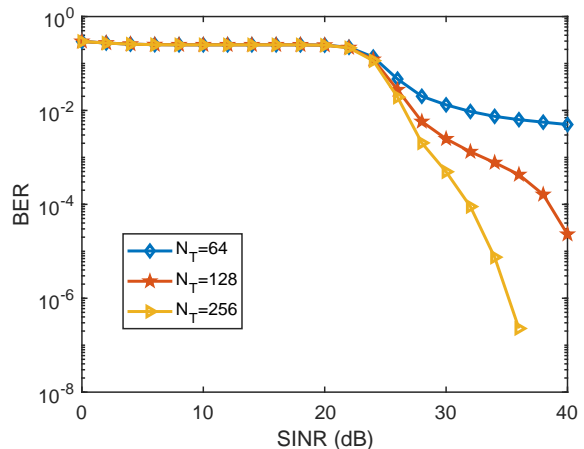


Fig. 13. The curve of BER versus SINR under different array sizes.

## VI. CONCLUSIONS

In this paper, we have proposed a practical ISAC framework to sense dynamic targets from clutter environment while ensuring users communications quality. In order to implement communications function and sensing function simultaneously, we have designed multiple communications beams that can communicate with the users and one rotating sensing beam

can scan the entire space. To minimize the interference of sensing beam on existing communications systems, we have divided the service area into S4S sectors and C4S sectors, and have provided beamforming design and power allocation optimization strategies for each type sector. Then we have proposed the clutter model for ISAC system in urban scenarios and have derived the sensing channel model that includes both static environment and dynamic targets. When BS received echo signals, MPC method was employed to filter out the static environmental clutter and to extract the effective dynamic target echoes. Then the task of dynamic target sensing is to detect the presence of dynamic targets and to estimate their angles, distances, and velocities parameters. Among them, dynamic target detection and angle estimation were realized through angle-Doppler spectrum estimation and joint detection over multiple subcarriers, while distance and velocity estimation were realized through the extended subspace algorithm. Simulation results have been provided to demonstrate the effectiveness of the proposed schemes and its superiority over the existing methods that ignore clutter environment.

## REFERENCES

- [1] F. Liu, Y. Cui, C. Masouros, J. Xu, T. X. Han, Y. C. Eldar, and S. Buzzi, "Integrated sensing and communications: Toward dual-functional wireless networks for 6G and beyond," *IEEE J. Sel. Areas Commun.*, vol. 40, no. 6, pp. 1728–1767, Jun. 2022.
- [2] M. Giordani, M. Polese, M. Mezzavilla, S. Rangan, and M. Zorzi, "Toward 6G networks: Use cases and technologies," *IEEE Commun. Mag.*, vol. 58, no. 3, pp. 55–61, Mar. 2020.
- [3] C. De Lima *et al.*, "Convergent communication, sensing and localization in 6G systems: An overview of technologies, opportunities and challenges," *IEEE Access*, vol. 9, pp. 26902–26925, Jan. 2021.
- [4] C. Chaccour, M. N. Soorki, W. Saad, M. Bennis, P. Popovski, and M. Debbah, "Seven defining features of terahertz (THz) wireless systems: A fellowship of communication and sensing," *IEEE Commun. Surveys Tuts.*, vol. 24, no. 2, pp. 967–993, Jan. 2022.
- [5] Z. Wei, F. Liu, C. Masouros, N. Su, and A. P. Petropulu, "Toward multi-functional 6G wireless networks: Integrating sensing, communication, and security," *IEEE Commun. Mag.*, vol. 60, no. 4, pp. 65–71, Apr. 2022.
- [6] J. Yang, C.-K. Wen, and S. Jin, "Hybrid active and passive sensing for SLAM in wireless communication systems," *IEEE J. Sel. Areas Commun.*, vol. 40, no. 7, pp. 2146–2163, Jul. 2022.
- [7] J. Yang and *et al.*, "Enabling plug-and-play and crowdsourcing SLAM in wireless communication systems," *IEEE Trans. Wireless Commun.*, vol. 21, no. 3, pp. 1453–1468, Mar. 2022.
- [8] H. Que, J. Yang, C.-K. Wen, S. Xia, X. Li, and S. Jin, "Joint beam management and SLAM for mmWave communication systems," *IEEE Trans. Commun.*, pp. 1–1, Jul. 2023.
- [9] H. Chen, H. Srieddeen, T. Ballal, H. Wymeersch, M.-S. Alouini, and T. Y. Al-Naffouri, "A tutorial on terahertz-band localization for 6G communication systems," *IEEE Commun. Surveys Tuts.*, vol. 24, no. 3, pp. 1780–1815, May 2022.
- [10] Z. Lin, T. Lv, J. A. Zhang, and R. P. Liu, "3D wideband mmwave localization for 5G massive MIMO systems," in *Proc. IEEE Global Commun. Conf. (GLOBECOM)*, Waikoloa, HI, USA, Dec. 2019, pp. 1–6.
- [11] O. Kanhere and T. S. Rappaport, "Position location for futuristic cellular communications: 5G and beyond," *IEEE Commun. Mag.*, vol. 59, no. 1, pp. 70–75, Jan. 2021.
- [12] X. Ma, T. Ballal, H. Chen, O. Aldayel, and T. Y. Al-Naffouri, "A maximum-likelihood TDOA localization algorithm using difference-of-convex programming," *IEEE Signal Process. Lett.*, vol. 28, pp. 309–313, Jan. 2021.
- [13] H. Chen, T. Ballal, N. Saeed, M.-S. Alouini, and T. Y. Al-Naffouri, "A joint TDOA-PDOA localization approach using particle swarm optimization," *IEEE Wireless Commun. Lett.*, vol. 9, no. 8, pp. 1240–1244, Aug. 2020.
- [14] H. Chen, T. Ballal, and T. Y. Al-Naffouri, "DOA estimation with non-uniform linear arrays: A phase-difference projection approach," *IEEE Wireless Commun. Lett.*, vol. 10, no. 11, pp. 2435–2439, Nov. 2021.
- [15] Z. Gao, Z. Wan, D. Zheng, S. Tan, C. Masouros, D. W. K. Ng, and S. Chen, "Integrated sensing and communication with mmWave massive MIMO: A compressed sampling perspective," *IEEE Trans. Wireless Commun.*, vol. 22, no. 3, pp. 1745–1762, Mar. 2023.
- [16] Z. Wang, X. Mu, and Y. Liu, "STARS enabled integrated sensing and communications," *IEEE Trans. Wireless Commun.*, pp. 1–1, Feb. 2023.
- [17] Y. Li, X. Wang, and Z. Ding, "Multi-target position and velocity estimation using OFDM communication signals," *IEEE Trans. Commun.*, vol. 68, no. 2, pp. 1160–1174, Feb. 2020.
- [18] P. Kumari, J. Choi, N. González-Prelcic, and R. W. Heath, "IEEE 802.11ad-based radar: An approach to joint vehicular communication-radar system," *IEEE Trans. Veh. Technol.*, vol. 67, no. 4, pp. 3012–3027, Apr. 2018.
- [19] X. Chen, Z. Feng, Z. Wei, X. Yuan, P. Zhang, J. Andrew Zhang, and H. Yang, "Multiple signal classification based joint communication and sensing system," *IEEE Trans. Wireless Commun.*, pp. 1–1, 2023.
- [20] X. Liu, T. Huang, N. Shlezinger, Y. Liu, J. Zhou, and Y. C. Eldar, "Joint transmit beamforming for multiuser MIMO communications and MIMO radar," *IEEE Trans. Signal Process.*, vol. 68, pp. 3929–3944, Jun. 2020.
- [21] D. Luo, Z. Ye, and J. Zhu, "Secure transmit beamforming for radar-communication systems using NOMA," *IEEE Commun. Lett.*, vol. 26, no. 11, pp. 2557–2561, Nov. 2022.
- [22] D. Cong, S. Guo, H. Zhang, J. Ye, and M.-S. Alouini, "Beamforming design for integrated sensing and communication systems with finite alphabet input," *IEEE Wireless Commun. Lett.*, vol. 11, no. 10, pp. 2190–2194, Oct. 2022.
- [23] Z. He, W. Xu, H. Shen, Y. Huang, and H. Xiao, "Energy efficient beamforming optimization for integrated sensing and communication," *IEEE Wireless Commun. Lett.*, vol. 11, no. 7, pp. 1374–1378, Jul. 2022.
- [24] C. B. Barneto, T. Riihonen, S. D. Liyanaarachchi, M. Heino, N. González-Prelcic, and M. Valkama, "Beamformer design and optimization for joint communication and full-duplex sensing at mm-Waves," *IEEE Trans. Commun.*, vol. 70, no. 12, pp. 8298–8312, Dec. 2022.
- [25] H. Luo, R. Liu, M. Li, Y. Liu, and Q. Liu, "Joint beamforming design for RIS-assisted integrated sensing and communication systems," *IEEE Trans. Veh. Technol.*, vol. 71, no. 12, pp. 13393–13397, Dec. 2022.
- [26] X. Wang, Z. Fei, J. A. Zhang, and J. Xu, "Partially-connected hybrid beamforming design for integrated sensing and communication systems," *IEEE Trans. Commun.*, vol. 70, no. 10, pp. 6648–6660, Oct. 2022.
- [27] H. Luo, F. Gao, W. Yuan, and S. Zhang, "Beam squint assisted user localization in near-field integrated sensing and communications systems," *IEEE Trans. Wireless Commun.*, pp. 1–1, Oct. 2023.
- [28] D. Shnidman, "Generalized radar clutter model," *IEEE Trans. Aerosp. Electron. Syst.*, vol. 35, no. 3, pp. 857–865, Jul. 1999.
- [29] J. Billingsley *et al.*, "Statistical analyses of measured radar ground clutter data," *IEEE Trans. Aerosp. Electron. Syst.*, vol. 35, no. 2, pp. 579–593, Apr. 1999.
- [30] D. Barton, "Land clutter models for radar design and analysis," *Proceedings of the IEEE*, vol. 73, no. 2, pp. 198–204, Feb. 1985.
- [31] M. I. Skolnik, "Radar handbook," 3rd ed. New York, NY, USA: McGraw-Hill, 2008.
- [32] C. Sturm and W. Wiesbeck, "Waveform design and signal processing aspects for fusion of wireless communications and radar sensing," *Proceedings of the IEEE*, vol. 99, no. 7, pp. 1236–1259, Jul. 2011.
- [33] T. Multerer, M. Vossiek, U. Prechtel, and V. Ziegler, "Spectrum-efficient real-time OFDM MIMO radar for moving target detection in medium-range applications," in *Proc. IEEE MTT-S Int. Microw. Symp. Dig.*, Munich, Germany, Aug. 2018, pp. 1–4.
- [34] H. Rohling, "Radar CFAR thresholding in clutter and multiple target situations," *IEEE Trans. Aerosp. Electron. Syst.*, vol. AES-19, no. 4, pp. 608–621, Jul. 1983.
- [35] M. Wax and T. Kailath, "Detection of signals by information theoretic criteria," *IEEE Trans. Acoust., Speech, Signal Process.*, vol. 33, no. 2, pp. 387–392, Apr. 1985.
- [36] A. Barron, J. Rissanen, and B. Yu, "The minimum description length principle in coding and modeling," *IEEE Trans. Inf. Theory*, vol. 44, no. 6, pp. 2743–2760, Oct. 1998.
- [37] K. B. S. A. Dapa, G. Point, S. Bensator, and F. E. Boukour, "Vehicular communications over OFDM radar sensing in the 77 GHz mmWave band," *IEEE Access*, vol. 11, pp. 4821–4829, Jan. 2023.